Extreme Mechanics Letters 54 (2022) 101716

Contents lists available at ScienceDirect

Extreme Mechanics Letters

journal homepage: www.elsevier.com/locate/eml

Multimaterial stress-constrained topology optimization with multiple distinct yield criteria

Rahul Dev Kundu [a], Weichen Li [a], Xiaojia Shelly Zhang [a,b,*]

[a] Department of Civil and Environmental Engineering, University of Illinois Urbana-Champaign, 205 North Mathews Ave, Urbana, IL 61801, USA
[b] Department of Mechanical Science and Engineering, University of Illinois Urbana-Champaign, USA

ARTICLE INFO

Article history:
Received 2 November 2021
Accepted 21 March 2022
Available online 22 April 2022

Keywords:
Multimaterial topology optimization
Stress constraint
Yield function interpolation
Volume minimization
Stress deconcentration
Tension–compression strength asymmetry

ABSTRACT

Composite structures offer unique mechanical and physical properties enabled by material heterogeneity. To harness these properties in stress-constrained topology optimization, the incorporation of multiple materials is necessary. Established studies in the field typically assume the same yield criterion for all the candidate materials while vary their stiffness and strengths. To open up the full design capability for composite structures, we propose a novel yield function interpolation scheme that allows for the simultaneous incorporation of distinct yield criteria and material strengths. Built upon this yield function interpolation scheme, we introduce a stress-constrained topology optimization formulation that handles multiple materials with distinct elastic properties, material strengths, and yield criteria simultaneously. We investigate several two-dimensional and three-dimensional design cases with the objective of minimizing the total volume subjected to stress constraints. The optimized composite designs reveal several fundamental advantages enabled by material heterogeneity, including design space enlargement, stress deconcentration effect, and exploitation of tension–compression strength asymmetry. These advantages lead to composite designs with $10-40\%$ reduced minimized volumes as compared to single-material designs and provide new insights for the discovery of more efficient composite structures.

1. Introduction

Composite structures are extensively used across various engineering fields owing to their superior mechanical and physical properties over single-material structures. The advantages inspire the use of multiple materials in topology optimization to achieve novel designs with superior performance. Till now, great advances have been achieved in developing versatile multimaterial topology optimization formulations [1–14] to discover composite structures with novel geometries and functionalities in various applications, such as multiphysics [15–19] and metamaterial/metastructure design [20–22] problems. In structural mechanics, popular design problems for multimaterial topology optimization include compliance minimization, compliant mechanism [5,9], inverse design for target mechanical behaviors [21,22], and stress-constrained design optimization [23,24].

Among these problems, multimaterial stress-constrained topology optimization is an important and challenging one, which has been investigated by relatively fewer studies. Existing stress-constrained formulations consider a variety of objectives such as compliance minimization [23,25], maximum stress minimization [25], compliant mechanism design [26], volume/mass minimization [23,24], and programming of nonlinear target responses [22]. In these studies, different candidate materials could take distinct elastic properties [22,23,25,26], yield strengths [22,23,25,26], and strength-to-density ratios [24]. However, all of them are governed by the same yield/failure criterion, e.g., von-Mises. Yet, the capability of accounting for distinct yield/failure criteria in different candidate materials is crucial for many applications, as many real-world composite structures are made of materials governed by distinct yield/failure criteria. For instance, in reinforced concrete structures, the steel rebars are governed by a hydrostatically-independent criterion, e.g., von-Mises, whereas the concrete is controlled by a hydrostatically-dependent criterion, e.g., Drucker–Prager. However, this capability has been rarely explored and is currently underdeveloped in multimaterial stress-constrained topology optimization.

To fill this gap, this work puts forward a multimaterial stress-constrained topology optimization formulation capable of accounting for multiple candidate materials with distinct elastic properties (i.e., stiffness), strengths, and yield/failure criteria simultaneously, see Fig. 1(a). This is achieved by the introduction

* Corresponding author at: Department of Civil and Environmental Engineering, University of Illinois Urbana-Champaign, 205 North Mathews Ave, Urbana, IL 61801, USA.
E-mail address: zhangxs@illinois.edu (X.S. Zhang).

https://doi.org/10.1016/j.eml.2022.101716
2352-4316/

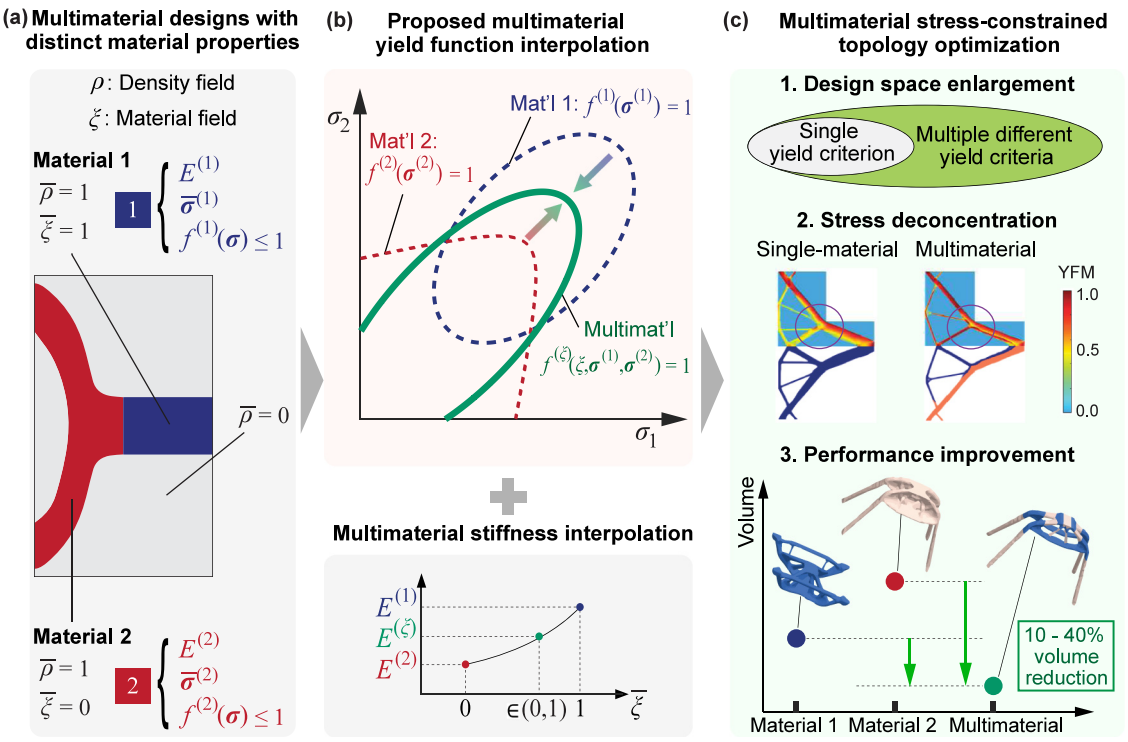

Fig. 1. Illustration of the overall goal of this study. (a) Design characterization of composite structures with different material elastic moduli, strengths, and yield criteria. (b) Proposed multimaterial yield function interpolation scheme and stiffness interpolation. (c) Multimaterial stress-constrained topology optimization framework with unique advantages produced by material heterogeneity: design space enlargement, stress deconcentration, and performance improvement.

of a novel yield function interpolation scheme, which effectively encodes various yield functions of different forms into the design parameterization (Fig. 1(b)). Using this proposed framework, we numerically investigate several two-dimensional (2D) and three-dimensional (3D) design problems that aim to minimize the total structural volume. The obtained optimized composite structures exhibit novel distributions of both geometry and material phases and demonstrate several unique advantages provided by material heterogeneity with different yield/failure criteria, including design space enlargement, stress deconcentration, and exploitation of tension–compression strength asymmetry, see Fig. 1(c). As a result, these advantages significantly reduce the optimized volume compared to single-material designs and provide general design guidelines for composite structures and materials where material constituents are governed by different yield/failure criteria.

The remainder of this paper is organized as follows. Section 2 introduces design parameterization of multimaterial structures and elaborates the proposed yield function interpolation scheme, after which the multimaterial stress-constrained topology optimization formulation is presented. Section 3 presents several design examples, including both 2D and 3D problems, to demonstrate the unique advantages enabled by the proposed formulation. Section 4 provides a few concluding remarks. Appendices (four sections) complement the paper with a brief description of design discretization and regularization, an elaboration of the effect of yield function interpolation parameter on optimized designs, sensitivity analysis required for gradient-based optimization, and values of algorithm parameters.

2. Methods

This section presents the multimaterial stress-constrained topology optimization framework that simultaneously considers distinct elastic moduli, yield strengths, and yield criteria. We first introduce the design parameterization of multimaterial structures and then focus on the proposed interpolation scheme for different yield functions, after which the optimization formulation and algorithm are presented.

2.1. Design parameterization of multimaterial structures

Design parameterization of multimaterial structures requires a density design field (denoted by $\rho(\boldsymbol{x})$) and a material design field (denoted by $\xi(\boldsymbol{x})$) [27,28]. The density field characterizes material spatial occupancy, with $\rho(\boldsymbol{x}) = 1$ and 0 indicating solid and void, respectively. The material field characterizes material types, with $\xi(\boldsymbol{x}) = 1$ and 0 representing Material 1 and Material 2, respectively. For numerical computation, we consider piecewise constant distributions for both fields which are represented by two design variable vectors denoted by $\boldsymbol{\rho}$ and $\boldsymbol{\xi}$, with ρ_e and ξ_e being the values associated with element e in the Finite Element Analysis (FEA). To regularize the design space, we apply the density filter [29–31] and projection [32] operations to the two design variables to generate their corresponding physical variables, $\bar{\boldsymbol{\rho}}$ and $\bar{\boldsymbol{\xi}}$, which are used to represent the physical multimaterial structures [22,32] (see Appendix A).

Through the two physical variables, the elasticity tensor $\mathbb{C}^{(\xi)}$ of element e is obtained by the Solid Isotropic Material with Penalization (SIMP) [27,33] through $\bar{\boldsymbol{\rho}}$ combined with a SIMP-like interpolation through $\bar{\boldsymbol{\xi}}$ [2,22,28], i.e.,

$$\mathbb{C}_e^{(\xi)}(\bar{\rho}_e, \bar{\xi}_e) = \left[\varepsilon + (1-\varepsilon)\bar{\rho}_e^{\,p_\rho}\right]\left[\bar{\xi}_e^{\,p_\xi}\mathbb{C}^{(1)} + \left(1-\bar{\xi}_e\right)^{p_\xi}\mathbb{C}^{(2)}\right]. \quad (1)$$

Here $\mathbb{C}^{(1)}$ and $\mathbb{C}^{(2)}$ are elastic tensors of Material 1 and Material 2, respectively, p_ρ and p_ξ are SIMP penalization parameters, and ε is a small number to avoid numerical singularity. This study uses $p_\rho = p_\xi = 3$, which are commonly adopted values in topology optimization studies [22,32,34]. It can be seen that, when $\bar{\rho}_e = 1$ and $\bar{\xi}_e = 1$, $\mathbb{C}_e^{(\xi)}$ reduces to $\mathbb{C}^{(1)}$; and when $\bar{\rho}_e = 1$ and

$\bar{\xi}_e = 0$, $\mathbb{C}_e^{(\xi)}$ reduces to $\mathbb{C}^{(2)}$. Notice that the interpolation (1) is a popular numerical scheme to facilitate the design optimization rather than computing the homogenized properties, and hence, $\mathbb{C}^{(\xi)}$ is physically well-defined only when $\bar{\rho}_e, \bar{\xi}_e \in \{0, 1\}$, which is enforced by the projection technique. Without loss of generality, we assume that Material 1 and Material 2 are both isotropic with Poisson's ratio $\nu = 0.3$. Hence, the interpolation (1) can be simplified to the interpolation of Young's moduli,

$$E_e^{(\xi)}(\bar{\rho}_e, \bar{\xi}_e) = \left[\varepsilon + (1-\varepsilon)\bar{\rho}_e{}^{p_\rho}\right]\left[\bar{\xi}_e{}^{p_\xi} E^{(1)} + \left(1-\bar{\xi}_e\right)^{p_\xi} E^{(2)}\right], \quad (2)$$

with $E^{(1)}$ and $E^{(2)}$ being Young's moduli of Material 1 and Material 2, respectively.

2.2. Interpolation of yield functions and strengths

This subsection introduces a yield function interpolation scheme that enables stress-constrained topology optimization using materials with distinct yield criteria and strengths. We first express the general yield criterion $f(\boldsymbol{\sigma})$ for an isotropic material as [35]:

$$f\left(I_1(\boldsymbol{\sigma}), J_2(\boldsymbol{\sigma}), J_3(\boldsymbol{\sigma})\right) \leq 1, \quad (3)$$

with $I_1(\boldsymbol{\sigma}) = \mathrm{tr}(\boldsymbol{\sigma})$, $J_2(\boldsymbol{\sigma}) = \frac{1}{2}\boldsymbol{s}(\boldsymbol{\sigma}) : \boldsymbol{s}(\boldsymbol{\sigma})$, $J_3(\boldsymbol{\sigma}) = \det(\boldsymbol{s}(\boldsymbol{\sigma}))$, where $\boldsymbol{\sigma}$ is the stress tensor, $\boldsymbol{s}(\boldsymbol{\sigma}) = \boldsymbol{\sigma} - \frac{1}{3}I_1(\boldsymbol{\sigma})\boldsymbol{I}$ is the deviatoric stress tensor, I_1 is the first invariant of the stress tensor $\boldsymbol{\sigma}$, J_2 and J_3 are the second and third invariants of the deviatoric stress tensor $\boldsymbol{s}$, respectively, and $\boldsymbol{I}$ is the identity tensor. Accordingly, the yield surface is determined by taking $f\left(I_1(\boldsymbol{\sigma}), J_2(\boldsymbol{\sigma}), J_3(\boldsymbol{\sigma})\right) = 1$. As two special cases of (3), the von-Mises [36] and Drucker–Prager [37] criteria can be expressed as:

$$f(\boldsymbol{\sigma}) = \frac{\sqrt{3J_2(\boldsymbol{\sigma})}}{\bar{\sigma}} \leq 1 \quad (4)$$

and

$$f(\boldsymbol{\sigma}) = \frac{\sqrt{J_2(\boldsymbol{\sigma})}}{A} - \frac{B}{A}I_1(\boldsymbol{\sigma}) \leq 1, \quad (5)$$

respectively, where $\bar{\sigma}$ is the strength for von-Mises material, $A = \frac{2}{\sqrt{3}}\left(\frac{\bar{\sigma}_c\bar{\sigma}_t}{\bar{\sigma}_c+\bar{\sigma}_t}\right)$ and $B = \frac{1}{\sqrt{3}}\left(\frac{\bar{\sigma}_t-\bar{\sigma}_c}{\bar{\sigma}_c+\bar{\sigma}_t}\right)$ are parameters of the Drucker–Prager material with $\bar{\sigma}_t$ and $\bar{\sigma}_c$ denoting the uniaxial tension and compression strengths, respectively.

While (3) is general, it does not account for multiple different yield criteria. Here, we propose a SIMP-like yield function interpolation scheme that simultaneously considers two (can be generalized to any number) distinct yield functions $f^{(1)}(\boldsymbol{\sigma}^{(1)})$ and $f^{(2)}(\boldsymbol{\sigma}^{(2)})$ for the two candidate materials. The interpolated yield function $f_e^{(\xi)}(\cdot)$ (associated with element e) takes the expression:

$$f_e^{(\xi)}\left(\bar{\xi}_e, \boldsymbol{\sigma}^{(1)}, \boldsymbol{\sigma}^{(2)}\right) = \bar{\xi}_e{}^{p_{f_\xi}} f^{(1)}(\boldsymbol{\sigma}^{(1)}) + \left(1-\bar{\xi}_e\right)^{p_{f_\xi}} f^{(2)}(\boldsymbol{\sigma}^{(2)}) \leq 1, \quad (6)$$

where $\boldsymbol{\sigma}^{(i)} \doteq \mathbb{C}^{(i)}\boldsymbol{\epsilon}^{(i)}$ is the stress tensor of the ith material with $\boldsymbol{\epsilon}^{(i)}$ being the linearized strain tensor, and p_{f_ξ} is the penalization parameter for the yield function interpolation. This study uses $p_{f_\xi} = 1$, which is chosen based on numerical investigations. More discussions on the appropriate p_{f_ξ} values are provided in Appendix B. Similarly to the interpolated elasticity tensor (1), the interpolated yield function $f_e^{(\xi)}$ recovers the yield function of $f^{(1)}$ and $f^{(2)}$ when $\bar{\rho}_e = 1, \bar{\xi}_e = 1$ and $\bar{\rho}_e = 1, \bar{\xi}_e = 0$, respectively. We remark that the proposed yield function interpolation scheme simultaneously accounts for different yield criteria and different yield strengths, as both information is encoded in the yield function of each candidate material.

This study assumes well-bonded material interfaces. The assumption is valid for materials that can form sufficiently strong chemical bonds at the interfaces. For example, cross-linking two Polydimethylsiloxane (PDMS) elastomers based on partial curing can develop high interfacial strengths and reduce the likelihood of interfacial failure, which is validated through experiments [38,39]. For materials that require adhesives to bond, interfacial failure could happen. In that case, considering interfacial strength in topology optimization warrants in-depth investigations, however, it is beyond the scope of this study.

2.3. Topology optimization formulation

Based on the proposed yield function interpolation (6), we present a multimaterial stress-constrained topology optimization formulation for volume minimization problems. To achieve faster convergence in optimization, we transform the original stress constraint (6) into an equivalent polynomial version [35]. The polynomial version imposes higher penalty when the stress constraint is severely violated and hence accelerates the search for a feasible optimization domain. The formulation in terms of design variables $\boldsymbol{\rho}$ and $\boldsymbol{\xi}$ is given by:

$$\begin{aligned}
\min_{\rho,\xi}\quad & V(\boldsymbol{\rho}) = \textstyle\sum_{e=1}^{N} \bar{\rho}_e(\boldsymbol{\rho}) v_e \\
\text{s.t.}\quad & g_e(\boldsymbol{\rho}, \boldsymbol{\xi}, \mathbf{U}(\boldsymbol{\rho}, \boldsymbol{\xi})) = [\varepsilon + (1-\varepsilon)\bar{\rho}_e(\boldsymbol{\rho})^{p_\rho}] \\
& \qquad (f_e^{(\xi)}(\boldsymbol{\xi}, \mathbf{U}(\boldsymbol{\rho}, \boldsymbol{\xi})) - 1) \\
& \qquad ((f_e^{(\xi)}(\boldsymbol{\xi}, \mathbf{U}(\boldsymbol{\rho}, \boldsymbol{\xi})) - 1)^2 + 1) \leq 0, \\
& \qquad e = 1, \ldots, N \\
& \rho_e, \xi_e \in [0, 1], \quad e = 1, \ldots, N \\
\text{with:}\quad & \mathbf{K}(\boldsymbol{\rho}, \boldsymbol{\xi})\mathbf{U} = \mathbf{F}_{\text{ext}},
\end{aligned} \quad (7)$$

where N is the total number of elements in the mesh, $\mathbf{K}(\boldsymbol{\rho}, \boldsymbol{\xi})$ is the global stiffness matrix obtained from the interpolated elasticity tensor in Eq. (1), $\mathbf{U}$ is the global displacement vector, and $\mathbf{F}_{\text{ext}}$ is the global external force vector. Notice that the formulation does not restrict the individual volume fraction of each candidate material in the design. Hence, the appearance and volume fractions of different materials in the final designs are determined solely by the tendency to achieve a lower objective function value.

The formulation (7) involves N nonlinear local stress constraints (corresponding to N finite elements) and, hence, is highly challenging to solve. In most studies, this challenge is bypassed by using aggregation methods (e.g., the p-norm approach [40]) where the N constraints are lumped into one or a handful of constraints. However, as stress is intrinsically local, aggregation approaches may cause numerical issues in the optimized designs [41]. More recently, the Augmented Lagrangian (AL) method [42,43], which preserves the local nature of stress constraints, has been used to successfully tackle single-material stress-constrained problems [35,44–53]. Therefore, the AL method is adopted in this study to solve the optimization problem (7).

The AL method solves a series of (augmented) unconstrained optimization sub-problems with penalty terms to approach the solution of the original constrained problem. At each step of the series, an unconstrained optimization problem is solved to update the design variables and penalty parameters. Specifically, at the kth optimization step, the corresponding unconstrained optimization sub-problem is formulated as [52]

$$\begin{aligned}
\min_{\boldsymbol{\rho}', \boldsymbol{\xi}'} \psi^{(k)}(\boldsymbol{\rho}', \boldsymbol{\xi}') = V(\boldsymbol{\rho}') + \frac{1}{N}\sum_{e=1}^{N}\Bigg[& \lambda_e^{(k)} h_e^{(k)}(\boldsymbol{\rho}', \boldsymbol{\xi}') \\
& + \frac{\mu^{(k)}}{2} h_e^{(k)}(\boldsymbol{\rho}', \boldsymbol{\xi}')^2\Bigg],
\end{aligned} \quad (8)$$

where $\psi^{(k)}(\boldsymbol{\rho}', \boldsymbol{\xi}')$ is the kth step (augmented) objective function with $\boldsymbol{\rho}'$ and $\boldsymbol{\xi}'$ denoting dummy design variables corresponding to

Table 1
Overview of numerical examples.

Example	Properties varied for different materials	Highlights
Ex. 1	E and $\bar{\sigma}$	Appearance and proportions of two materials, stress deconcentration effect, volume reduction due to stiffness heterogeneity
Ex. 2	$\bar{\sigma}$ and $f(\boldsymbol{\sigma})$	Distinct yield criteria, distinct optimized designs for different materials, volume reduction by exploitation of tension–compression strength asymmetry
Ex. 3	E, $\bar{\sigma}$ and $f(\boldsymbol{\sigma})$	Three-dimensional problem, distinct stiffness, strengths, and yield criteria

$\boldsymbol{\rho}$ and $\boldsymbol{\xi}$, $h_e(\boldsymbol{\rho}', \boldsymbol{\xi}')$ is the equality constraint for eth element given by

$$h_e^{(k)}(\boldsymbol{\rho}', \boldsymbol{\xi}') = \max\left(g_e(\boldsymbol{\rho}', \boldsymbol{\xi}', \mathbf{U}(\boldsymbol{\rho}', \boldsymbol{\xi}')), -\frac{\lambda_e^{(k)}}{\mu^{(k)}}\right), \tag{9}$$

where $\lambda_e^{(k)}$ are the Lagrange multiplier estimators, and $\mu^{(k)}$ is a penalty coefficient. The solution of the unconstrained problem (8) updates the design variables, i.e., $\boldsymbol{\rho}^{(k+1)} = \boldsymbol{\rho}'^{*}$ and $\boldsymbol{\xi}^{(k+1)} = \boldsymbol{\xi}'^{*}$, which are then used to update the penalty parameters through

$$\begin{aligned}\mu^{(k+1)} &= \min\left(\alpha\mu^{(k)}, \mu_{\max}\right) \text{ and } \lambda_e^{(k+1)} \\ &= \lambda_e^{(k)} + \mu^{(k)} h_e^{(k)}\left(\boldsymbol{\rho}^{(k+1)}, \boldsymbol{\xi}^{(k+1)}\right),\end{aligned} \tag{10}$$

where $\alpha > 1$ is a constant penalty update factor and $\mu_{\max}$ is an upper bound of the penalty coefficient to prevent numerical instability. The unconstrained sub-problem is solved by the gradient-based Method of Moving Asymptotes [54]. The expressions of the gradients with respect to the design variables are provided in Appendix C.

3. Results and discussions

This section presents three numerical examples of optimized multimaterial designs obtained with the proposed yield function interpolation scheme. The first example focuses on stress deconcentration effect produced by stiffness heterogeneity. The second example demonstrates the efficient utilization of available candidate materials with different yield criteria. The third example extends the proposed methodology to a complex 3D problem. The three examples demonstrate unique advantages of material heterogeneity (i.e., variation in Young's modulus E, yield strength $\bar{\sigma}$, and yield criterion $f(\boldsymbol{\sigma})$) from different perspectives. A summary of the highlights and features of these examples is given in Table 1.

The optimization is terminated when a prescribed maximum number of AL steps is reached or a prescribed tolerance for the stress constraints is achieved after the projections of design variables are applied. The values of the AL parameters and convergence tolerances for all numerical examples are provided in Appendix D.

3.1. Ex.1: Designs with distinct stiffness and strengths

The first example reveals two key parameters governing the appearance and relative portions of different materials in optimized designs. It also illustrates the unique stress deconcentration effect produced by material stiffness heterogeneity, which yields multimaterial designs with significantly lower volumes than single-material designs. This example considers two candidate materials (labeled as Material 1 and Material 2, respectively) both governed by the von-Mises criterion but with different elastic moduli and yield strengths. Using the two materials, we investigate five design cases with a corbel design domain as shown in Fig. 2(a). Different material parameters are listed in Fig. 2(b). The first three cases (Dsg. 1 to 3) use two materials with increasing yield strength in Material 2. The other two cases (Dsg. 3 A and 3B) use single materials with properties identical to Dsg. 3. The obtained optimized designs with density and material filter radii $R_\rho = R_\xi = 190.0$ mm are shown in Fig. 2(c) along with their fringe plots of yield function measure (YFM) (defined as $\left[\varepsilon + (1-\varepsilon)\bar{\rho}_e^{p_\rho}\right] f_e^{(\xi)}$) and principal stress distributions relative to the yield surfaces. The yield surface plots demonstrate the satisfaction of stress constraints within all structures.

With Dsgs. 1 to 3, we show that the appearance and relative portions of the two materials depend not only on the relative yield strengths but also on the strength-to-stiffness ratios of different materials denoted by ϕ. On the one hand, the influence of the relative yield strengths is demonstrated by Dsg. 1 where only Material 1 with higher yield strength but the same ϕ appears as it allows for higher stress in the design as compared to Material 2. On the other hand, the influence of the strength-to-stiffness ratio ϕ is demonstrated by Dsg. 2 where Material 2 with the lower yield strength but higher ϕ value appears in the two re-entrant corners. In general, the material with higher values of $\bar{\sigma}$ and ϕ occupies a larger portion in the optimized designs. This trend is shown by comparing Dsgs. 1 to 3, where the increase of these two quantities in Material 2 raises its portion in the optimized structures.

Furthermore, the material with higher values in $\bar{\sigma}$ and ϕ does not exclusively occupy the final designs. As shown in Dsg. 3, although Material 2 has higher $\bar{\sigma}$ and ϕ than Material 1, Material 1 remains in the optimized design. This reveals a stress deconcentration effect enabled by stiffness heterogeneity that can be harnessed to further reduce the volume of the design. To illustrate this stress deconcentration effect, we investigate two single-material designs (Dsg. 3A and 3B) with material properties (elastic moduli and yield strengths) identical to those in Dsg. 3. As shown in Fig. 2(c), the volume of the composite Dsg. 3 is 31% and 9% lower than the single-material Dsgs. 3A and 3B, respectively. The reduction in volume comes from a stress deconcentration effect enabled by stiffness heterogeneity, which can be elucidated by comparing the YFM fringe plots of the three designs. In the single-material designs (Dsg. 3A and 3B), the internal parts of the optimized structures are under-stressed with YFM values lower than 0.7, while their outer parts are close to maximum stress limits of the corresponding materials with YFM values equal to 1. Although the substantial amount of unused strength capacity in the internal parts may indicate inefficient material usage, these internal members cannot be arbitrarily reduced in size or removed because doing so would increase the stress level in those severely-stressed outer regions and lead to violation of the stress constraint in those regions. By contrast, the inefficiency is alleviated in the multimaterial design (Dsg. 3). As shown in the fringe plot of Dsg. 3, the YFM is distributed much more evenly with values close to 1, representing a less concentrated stress state in outer regions. This stress deconcentration effect is achieved by combining materials with different stiffness within the structure so that the stiffer material placed in regions that tend to be under-stressed can partially unload stress in regions that tend to get higher stress. By harnessing this stress deconcentration mechanism enabled by stiffness heterogeneity, the proposed multimaterial framework generates a composite structure with lower volume compared to single-material structures made of either of its constituent material.

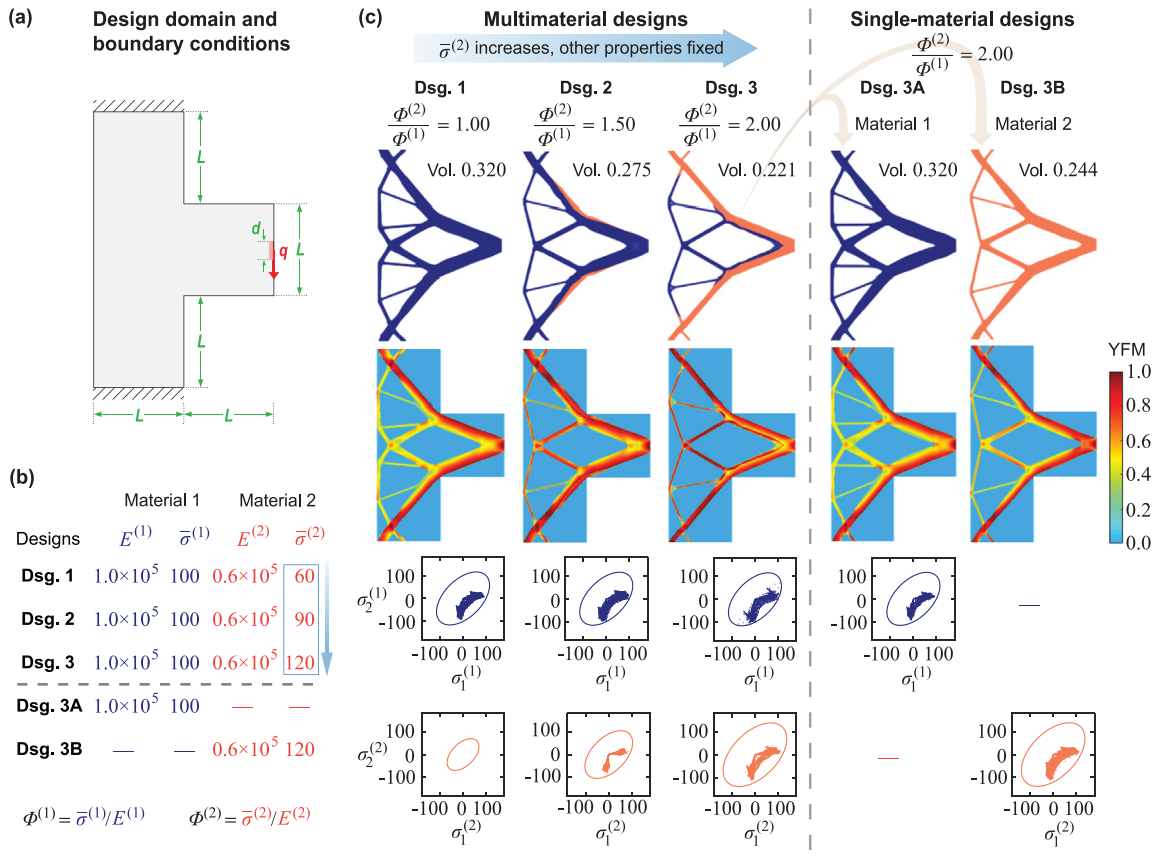

Fig. 2. Stress deconcentration in optimized multimaterial designs. (a) Design domain and boundary conditions (BCs), $L = 2.0 \times 10^3$ mm, $d = 4.0 \times 10^2$ mm, $q = 5.3 \times 10^4$ N/mm. (b) Material properties used for the designs (units: N and mm). (c) Multimaterial and single-material designs, corresponding YFM distributions, and principal stresses with yield surfaces.

3.2. Ex.2: Designs with distinct strengths and yield criteria

The second design example presents structures optimized considering multiple materials governed by distinct yield criteria and demonstrates enhancement of structural performance enabled by tension–compression strength asymmetry. The design domain and prescribed boundary conditions are shown in Fig. 3(a). For this design problem, we consider two materials with the same elastic moduli governed by von-Mises and Drucker–Prager yield criteria, respectively. The values of material properties are listed in Fig. 3(b). Notice that, the tension and compression strengths of the von-Mises material are identical; whereas the compression strength of the Drucker–Prager material is higher than the tension one. Filter radii $R_\rho = R_\xi = 50.0$ mm are used for all three designs.

In this example, we investigate three design scenarios. The first and second designs only consider the von-Mises material (Dsg. VM), and the Drucker–Prager material (Dsg. DP), respectively. The third design considers both von-Mises and Drucker–Prager materials by adopting the proposed yield function interpolation scheme (6). These three optimized designs are shown in Fig. 3(c) along with their YFM plots and principal stresses.

The three optimized designs considering different yield criteria show distinct geometries, which is caused by the different tension–compression symmetry properties of the von-Mises and Drucker–Prager criteria. As shown in Fig. 3(c), Dsg. VM forms two vertical tension members to connect the upper rollers and has no structural members attached to the bottom supports. This is because forming members to connect the upper rollers yields a shorter load path than forming members to reach the bottom supports. Moreover, the high tension strength in von-Mises material allows those vertical tension members to have small cross-sectional areas in order to minimize volume. By contrast, because such a high tension strength is unavailable in the Drucker–Prager material, compression members are favored in the Dsg. DP over tension ones in order to reduce their cross-sectional areas. As a result, Dsg. DP forms two inclined columns attached to the bottom supports and has no tension members connected to the upper rollers, leading to a structural configuration distinct from Dsg. VM. Notice that, although Dsg. DP has a slightly longer load path than Dsg. VM, their optimized volumes are almost identical. This is because the structural members in the Dsg. DP have relatively smaller cross-sectional areas enabled by the higher compression strength of the Drucker–Prager material compared to the von-Mises one.

The two-material design (Dsg. VM-DP) attains a structural configuration which combines features from both optimized single-material designs. As shown in Fig. 3(c), both the tension members, which are made of von-Mises material and connected to the upper rollers, and the compression columns, which are made of Drucker–Prager material and connected to the bottom supports, are present in Dsg. VM-DP. We remark that such a two-material design cannot be achieved by considering two candidate materials both of which are governed by either von-Mises or Drucker–Prager criteria. The optimized volume of the two-material design (Dsg. VM-DP) is approximately 10% lower than those of the two single-material ones, which is a result of the enlarged design space and the suitable exploitation of the tension–compression symmetry properties of the different yield criteria for the candidate materials. Moreover, the two-material Dsg. VM-DP along with its further reduced volume demonstrates

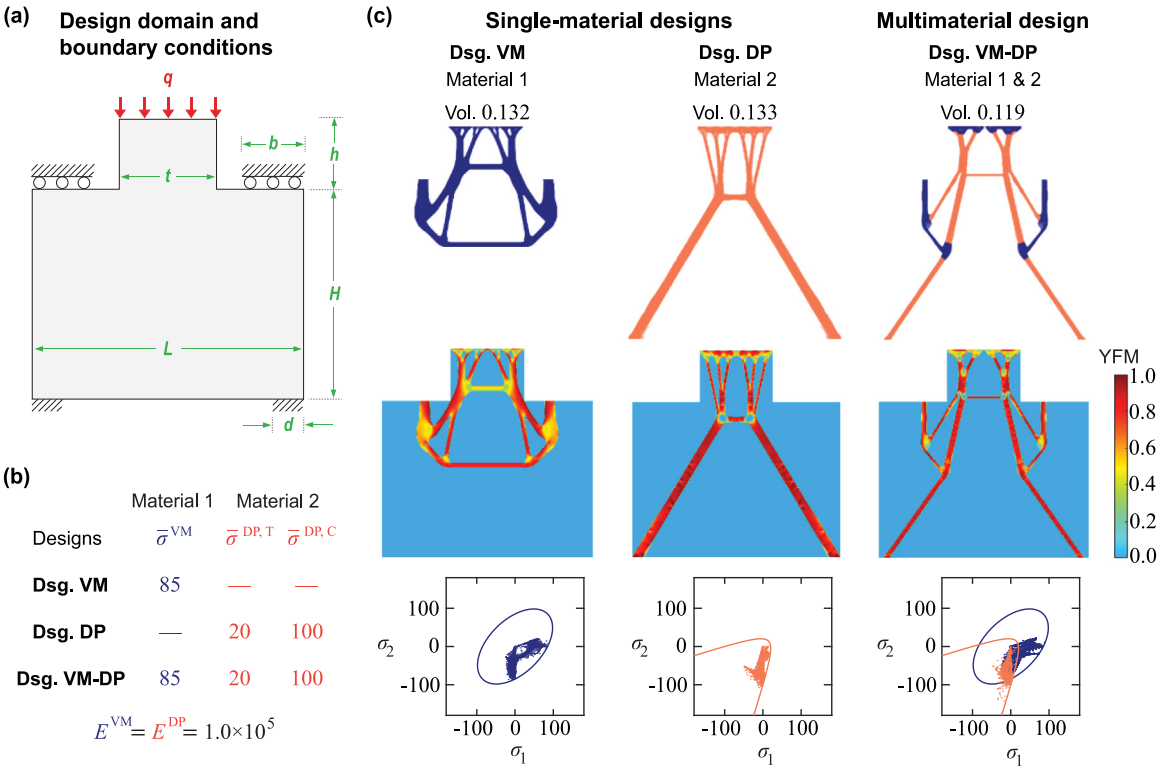

Fig. 3. Multimaterial design with von-Mises and Drucker–Prager type materials. (a) Design domain and BCs, $L = 2.0 \times 10^3$ mm, $H = 1.5 \times 10^3$ mm, $t = 7 \times 10^2$ mm, $b = 4.5 \times 10^2$ mm, $h = 5.0 \times 10^2$ mm, $d = 1.0 \times 10^2$ mm, $q = 1.9 \times 10^4$ N/mm. (b) Material properties used for the designs (units: N and mm). (c) Single-material and multimaterial designs, corresponding YFM distributions, and principal stresses with yield surfaces.

the effectiveness of the yield function interpolation and the unique advantages of using multiple candidate materials with different yield criteria.

3.3. Ex.3: 3D designs with distinct stiffness, strengths, and yield criteria

This example presents 3D multimaterial structures optimized using two candidate materials with distinct elastic moduli, yield strengths, and yield criteria (Tresca [55] and Mohr–Coulomb [56]). Tresca criterion is hydrostatically-independent and has identical tension and compression strengths, and it is mainly used for metals; whereas Mohr–Coulomb criterion is hydrostatically-dependent and has a tension strength considerably lower than compression strength, which is typically used for quasi-brittle materials. For comparison, we investigate designs optimized with Tresca material only (Dsg. TR), Mohr–Coulomb material only (Dsg. MC), and both materials (Dsg. TR-MC). The design domain (discretized by approximately 322K hexahedral elements) and boundary conditions are shown in Fig. 4(a). The properties of both Tresca (Material 1) and Mohr–Coulomb (Material 2) materials are listed in Fig. 4(b). The optimized designs with filter radii $R_\rho = R_\xi = 40.0$ mm of the three cases are shown in Fig. 4(c) along with their corresponding YFM fringe plots and principal stresses.

The three optimized designs exhibit distinct geometries and material distributions, which are caused by the different shapes of the two yield surfaces. Dsg. TR forms four tension members which connect to the top supports to sustain the load and has no members connecting to the bottom supports as they would increase total structural volume due to longer load paths. By contrast, Dsg. MC generates four inclined columns which are under compression to attach to the bottom supports and forms no tension members connecting to the top supports because those members would require much larger cross-section area (and hence total volume) as a result of the low tension strength of the Mohr–Coulomb material. The inefficiency of tension members is demonstrated at the lower chords of Dsg. MC, which have wide, plate-like cross-sections that lead to a 55% increase in total volume compared to Dsg. TR. The two-material Dsg. TR-MC forms four compression columns made of the Mohr–Coulomb material, which is similar to Dsg. MC, but the lower chords are made of Tresca material and hence possess a considerably smaller cross-section area compared to Dsg. MC. The optimized geometry and distribution of the two distinct materials produce a total structural volume lower than those of Dsg. TR and Dsg. MC, demonstrating the advantage of combining multiple materials to achieve higher structural efficiency.

4. Conclusions

This study puts forth a multimaterial stress-constrained topology optimization formulation with the objective of minimizing total structural volume. The main innovation of the formulation lies in its capability of simultaneously handling multiple candidate materials with distinct elastic properties, strengths, and yield criteria, the latter of which has been rarely investigated in existing work. To enable this capacity, a novel yield function interpolation scheme is proposed to handle multiple candidate materials not only having different yield/failure strengths but also governed by different yield criteria (with distinct forms of yield functions) in a unified manner. An AL algorithm, which preserves the local nature of the stress constraint, is employed to efficiently solve the optimization problem with many constraints.

Using the proposed formulation, we investigate several 2D and 3D design cases and obtain optimized structures with unconventional geometries and material phase distributions. The

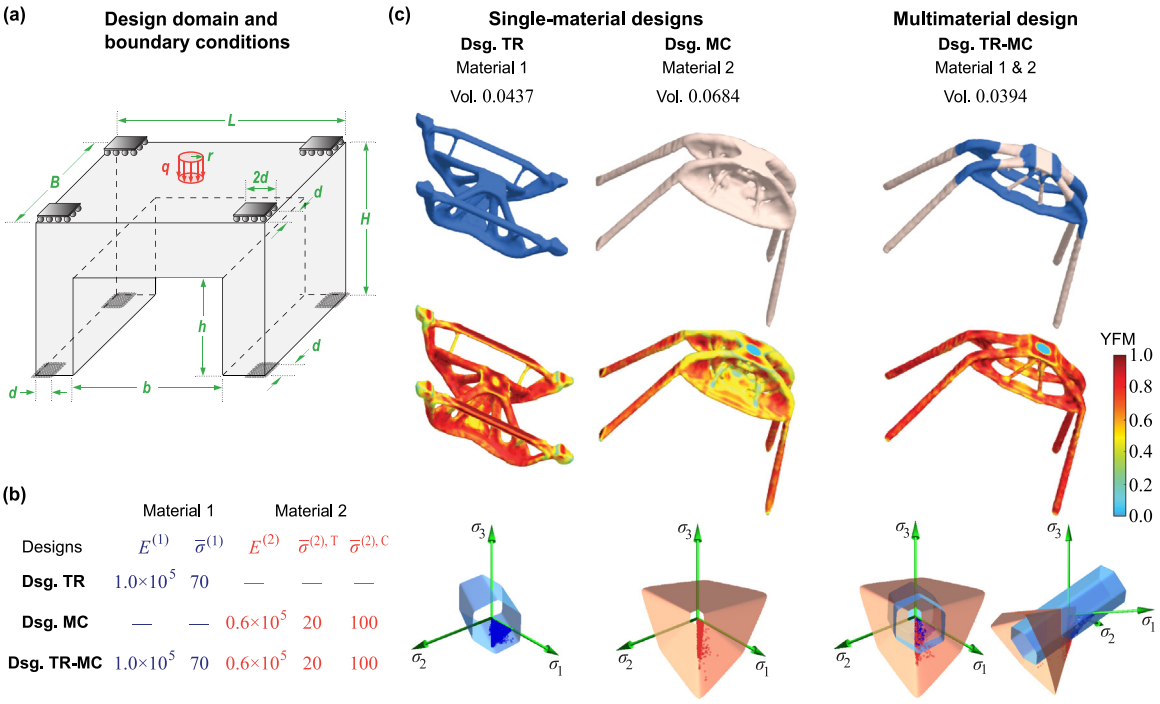

Fig. 4. Multimaterial design with Tresca and Mohr–Coulomb type materials. (a) Design domain and BCs, $L = 1.5 \times 10^3$ mm, $H = 1.0 \times 10^3$ mm, $B = 7.5 \times 10^2$ mm, $b = 1.0 \times 10^3$ mm, $h = 6.5 \times 10^2$ mm, $d = 1.0 \times 10^2$ mm, $r = 5.0 \times 10^1$ mm, $q = 76.4$ N/mm^2. (b) Material properties used for the designs, (units: N and mm). (c) Single-material and multimaterial designs, corresponding YFM distributions, and principal stresses with yield surfaces.

optimized designs reveal several fundamental advantages provided by heterogeneity in stiffness, strength, and yield/failure criteria, including the enlarged design space achieved by the inclusion of different yield criteria, the stress deconcentration effect enabled by stiffness and strength heterogeneity, and the exploitation of diverse tension–compression symmetry/asymmetry in both hydrostatically-independent and -dependent materials. These unique advantages are comprehensively and effectively harnessed by the proposed formulation to generate optimized composite designs with significantly improved structural efficiency and reduced structural volume relative to single-material structures. The findings facilitate the discovery of better and more efficient composite structures across various fields.

Declaration of competing interest

The authors declare that they have no known competing financial interests or personal relationships that could have appeared to influence the work reported in this paper.

Acknowledgments

The authors would like to devote this paper to the Special Issue in honor of Professor Glaucio H. Paulino on the occasion of receiving the 2020 ASME Daniel C. Drucker Medal. The authors would like to acknowledge the financial supports through the U.S. National Science Foundation (NSF) EAGER grant CMMI-2127134 and NSF CAREER Award CMMI-2047692, USA. The information provided in this paper is the sole opinion of the authors and does not necessarily reflect the view of the sponsoring agencies.

Appendix A. Projection and filter of design variables

Projection [32] and filter [31] are common techniques in topology optimization used to achieve mesh-independent and discrete designs [31,34]. The physical variables are obtained by the smoothed Heaviside projection [22,32] through

$$\bar{\rho}_e = \frac{\tanh(\beta_\rho \eta_\rho) + \tanh(\beta_\rho(\tilde{\rho}_e - \eta_\rho))}{\tanh(\beta_\rho \eta_\rho) + \tanh(\beta_\rho(1 - \eta_\rho))} \quad \text{and}$$
$$\bar{\xi}_e = \frac{\tanh(\beta_\xi \eta_\xi) + \tanh(\beta_\xi(\tilde{\xi}_e - \eta_\xi))}{\tanh(\beta_\xi \eta_\xi) + \tanh(\beta_\xi(1 - \eta_\xi))} \tag{A.1}$$

where the projection discreteness is regulated by the Heaviside parameters β_ρ and β_ξ, and the projection thresholds η_ρ and η_ξ, and $\tilde{\boldsymbol{\rho}}$ and $\tilde{\boldsymbol{\xi}}$ are intermediate filtered variables [29,30] obtained by:

$$\tilde{\rho}_e = \frac{\sum_{j \in \mathrm{n_e}(R_\rho)} w\left(\boldsymbol{x}_j\right) v_j \rho_j}{\sum_{j \in \mathrm{n_e}(R_\rho)} w\left(\boldsymbol{x}_j\right) v_j} \quad \text{and} \quad \tilde{\xi}_e = \frac{\sum_{j \in \mathrm{n_e}(R_\xi)} w\left(\boldsymbol{x}_j\right) v_j \xi_j}{\sum_{j \in \mathrm{n_e}(R_\xi)} w\left(\boldsymbol{x}_j\right) v_j} \tag{A.2}$$

where $\boldsymbol{x}_j$ is the location of the centroid of element j, v_j is the corresponding element volume, $\mathrm{n_e}$ is the neighborhood of element defined by a filter radius R, i.e., $\mathrm{n_e}(R) = \left\{j : \left\|\boldsymbol{x}_j - \boldsymbol{x}_e\right\| \leq R\right\}$, $w\left(\boldsymbol{x}_j\right)$ is the cubic weight function defined as $w\left(\boldsymbol{x}_j\right) = \max\left(0, 1 - \frac{\|\boldsymbol{x}_j - \boldsymbol{x}_e\|_2}{R}\right)^3$, and R_ρ and R_ξ are the filter radii for density and material design variables, respectively.

Appendix B. Effect of parameter p_{f_ξ} in yield function interpolation

The parameter p_{f_ξ} in the proposed yield function interpolation (6) can impact the final optimized designs. Here, we study and demonstrate this impact, discuss its underlying mechanism, and justify the value ($p_{f_\xi} = 1$) used in all the numerical examples. To this end, we use three different values of p_{f_ξ}, i.e., $p_{f_\xi} = 0.5$, 1, and 1.5 and show their associated interpolated yield surfaces with $\bar{\xi} = 0.2$, 0.5, and 0.8, respectively. We also compare the three corresponding optimized designs in terms of their final volumes, YFM fringe plots, principal stress distributions, and the

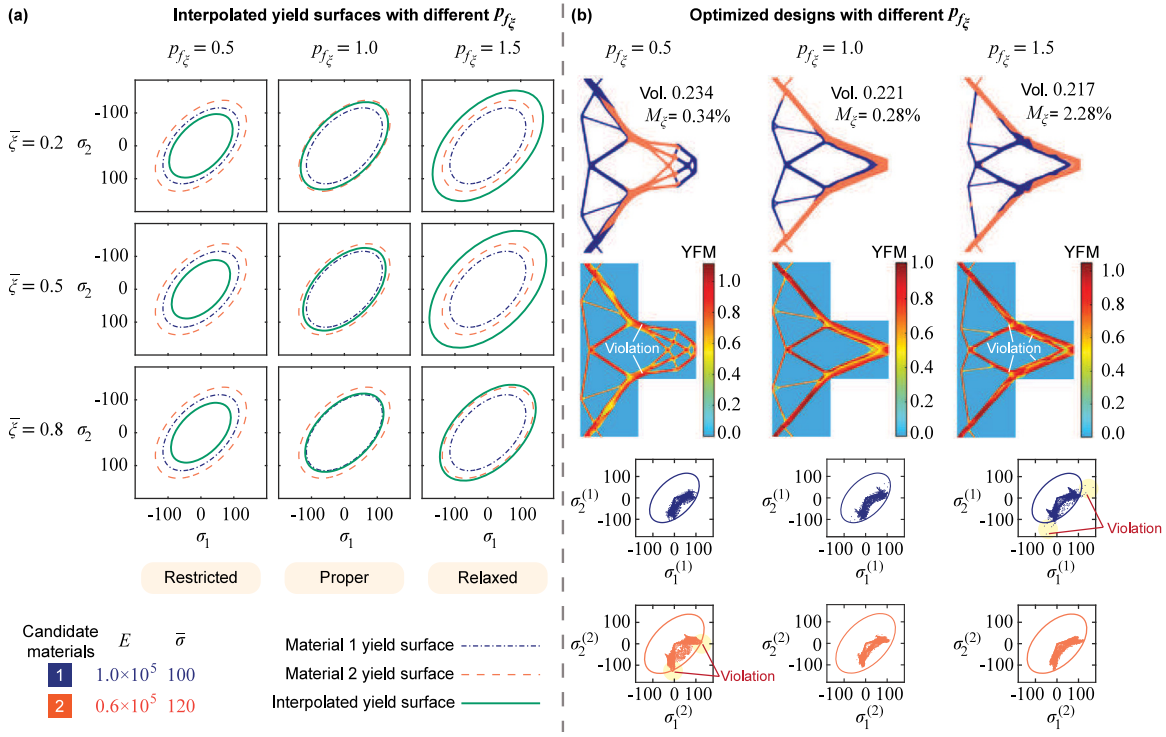

Fig. B.5. Effect of parameter $p_{f_{\bar{\xi}}}$ in yield function interpolation. (a) Interpolated yield surfaces for different values of $p_{f_{\bar{\xi}}}$ and $\bar{\xi}$, E and $\bar{\sigma}$ are in MPa. (b) Optimized multimaterial designs for different values of $p_{f_{\bar{\xi}}}$, corresponding YFM distributions, and principal stresses with yield surfaces.

extent of intermediate material remaining in the final optimized designs. The parameter $M_{\bar{\xi}}$ represents the amount of intermediate materials in the optimized design and it is calculated as [31] $M_{\bar{\xi}} = \frac{1}{N_S}\sum_{e\in S} 4\bar{\xi}_e\left(1-\bar{\xi}_e\right) \times 100\%$, where S is the element set with $\bar{\rho} > 0.01$ and N_S is the number of elements that belong to S.

Fig. B.5(a) illustrates the influence of parameter $p_{f_{\bar{\xi}}}$ on the shape of interpolated yield surface for various levels of material mixing (characterized by $\bar{\xi}$ values). For $p_{f_{\bar{\xi}}} = 0.5$, the interpolated yield surface is contained by the two material yield surfaces for $\bar{\xi} = 0.2$, 0.5, and 0.8. This restricted interpolation reduces the stress limit in mixed materials existing during the early stage of the optimization, which could result in higher objective function value compared to the case $p_{f_{\bar{\xi}}} = 1$. For $p_{f_{\bar{\xi}}} = 1$, the interpolated yield surface lies between the yield surfaces of Material 1 and Material 2 for all $\bar{\xi}$ values and hence represents a proper interpolation of strengths. For $p_{f_{\bar{\xi}}} = 1.5$, the interpolated yield surface is relaxed and excluded from yield surfaces of the two materials and overestimates the stress limits in mixed materials. This can lead to violation of the local stress constraints in the optimized designs.

Fig. B.5(b) demonstrates the influence of parameter $p_{f_{\bar{\xi}}}$ on the optimized multimaterial designs. The restricted interpolation ($p_{f_{\bar{\xi}}} = 0.5$) induces excess penalization of stresses for intermediate materials at the early stage of optimization, and leads to an optimized design with higher volume compared to the design with proper interpolation ($p_{f_{\bar{\xi}}} = 1$). By contrast, the relaxed interpolation ($p_{f_{\bar{\xi}}} = 1.5$) promotes material removal by overestimating stress limits in mixed materials, and leads to an optimized design with volume slightly lower than that with proper interpolation ($p_{f_{\bar{\xi}}} = 1$). However, the relaxed interpolation contains almost 8 times more intermediate materials in the final design compared to the proper interpolation with the same $\beta_{\bar{\xi}}$. Moreover, we observe that the relaxed and restricted interpolations tend to cause stress-constraint violations for Material 1 and 2, respectively, which are indicated by corresponding maximum YFM values surpassing 1 and principal stresses residing outside the material yield surfaces.

Appendix C. Sensitivity analysis

Gradient-based design updates require the sensitivity of the AL function in Eq. (8). Here, we present the detailed expression of the sensitivity for the proposed multimaterial formulation. The sensitivity of the AL function with respect to $\boldsymbol{\rho}$ and $\boldsymbol{\xi}$ is obtained through the chain rule:

$$\frac{\partial \psi^{(k)}}{\partial \rho_e} = \sum_{i=1}^{N} \frac{\partial \psi^{(k)}}{\partial \bar{\rho}_i}\frac{\partial \bar{\rho}_i}{\partial \tilde{\rho}_i}\frac{\partial \tilde{\rho}_i}{\partial \rho_e} \tag{C.3}$$

$$\frac{\partial \psi^{(k)}}{\partial \xi_e} = \sum_{i=1}^{N} \frac{\partial \psi^{(k)}}{\partial \bar{\xi}_i}\frac{\partial \bar{\xi}_i}{\partial \tilde{\xi}_i}\frac{\partial \tilde{\xi}_i}{\partial \xi_e} \tag{C.4}$$

The second and third terms of the R.H.S. of the Eqs. (C.3) and (C.4) can be computed based on (A.1) and (A.2), respectively. Thus, the main complication lies in the first terms. They are computed through

$$\frac{\partial \psi^{(k)}}{\partial \bar{\rho}_e} = \frac{v_e}{\sum_{k=1}^{N} v_k} + \frac{1}{N}\left\{\left[\lambda_e^{(k)} + \mu^{(k)} h_e^{(k)}\right]\frac{\partial h_e^{(k)}}{\partial \bar{\rho}_e} + \boldsymbol{\Lambda}^T\left(\frac{\partial \mathbf{F}_{\text{int}}}{\partial \bar{\rho}_e}\right)\right\} \tag{C.5}$$

$$\frac{\partial \psi^{(k)}}{\partial \bar{\xi}_e} = \frac{1}{N}\left\{\left[\lambda_e^{(k)} + \mu^{(k)} h_e^{(k)}\right]\frac{\partial h_e^{(k)}}{\partial \bar{\xi}_e} + \boldsymbol{\Lambda}^T\left(\frac{\partial \mathbf{F}_{\text{int}}}{\partial \bar{\xi}_e}\right)\right\} \tag{C.6}$$

where $\boldsymbol{\Lambda}$ is the adjoint vector obtained by solving the adjoint system:

$$\mathbf{K}\boldsymbol{\Lambda} = -\sum_{e=1}^{N}\left[\lambda_e^{(k)} + \mu^{(k)} h_e^{(k)}\right]\frac{\partial h_e^{(k)}}{\partial \mathbf{U}} \tag{C.7}$$

For the linear material model considered in our study, the gradients of internal force $\mathbf{F}_{\text{int}}$ with respect to the physical variables can be expressed using the solid material stiffness matrices $\mathbf{k}_{0,e}^{(1)}$, $\mathbf{k}_{0,e}^{(2)}$, and displacement vector $\mathbf{u}_e$ for the eth element as:

$$\frac{\partial \mathbf{F}_{\text{int}}}{\partial \bar{\rho}_e} = [(1-\epsilon)p_\rho \bar{\rho}_e^{p_\rho - 1}]\left(\bar{\xi}_e^{p_\xi}\mathbf{k}_{0,e}^{(1)} + (1-\bar{\xi}_e)^{p_\xi}\mathbf{k}_{0,e}^{(2)}\right)\mathbf{u}_e \tag{C.8}$$

$$\frac{\partial \mathbf{F}_{\text{int}}}{\partial \bar{\xi}_e} = [\epsilon + (1-\epsilon)\bar{\rho}_e^{p_\rho}]\left(p_\xi \bar{\xi}_e^{p_\xi - 1}\mathbf{k}_{0,e}^{(1)} - p_\xi(1-\bar{\xi}_e)^{p_\xi - 1}\mathbf{k}_{0,e}^{(2)}\right)\mathbf{u}_e \tag{C.9}$$

The gradients of equality constraints $h_e^{(k)}$ vanish when $g_e^{(k)} < -\frac{\lambda_e^{(k)}}{\mu^{(k)}}$; otherwise, they are computed through (superscript k is omitted hereafter because all the operations are carried out in same kth AL step):

$$\frac{\partial h_e}{\partial \bar{\rho}_e} = \frac{\partial g_e}{\partial \bar{\rho}_e} = [(1-\epsilon)p_\rho \bar{\rho}_e^{p_\rho - 1}](f_e^{(\xi)} - 1)((f_e^{(\xi)} - 1)^2 + 1) \tag{C.10}$$

$$\frac{\partial h_e}{\partial \bar{\xi}_e} = \frac{\partial g_e}{\partial \bar{\xi}_e} = [\epsilon + (1-\epsilon)\bar{\rho}_e^{p_\rho}](3(f_e^{(\xi)} - 1)^2 + 1)\frac{\partial f_e^{(\xi)}}{\partial \bar{\xi}_e} \tag{C.11}$$

$$\frac{\partial h_e}{\partial \mathbf{U}} = \frac{\partial g_e}{\partial \mathbf{U}} = [\epsilon + (1-\epsilon)\bar{\rho}_e^{p_\rho}](3(f_e^{(\xi)} - 1)^2 + 1)\frac{\partial f_e^{(\xi)}}{\partial \mathbf{U}} \tag{C.12}$$

Finally, the gradients of $f^{(\xi)}$ with respect to the physical material variable $\bar{\xi}$ and state variable $\mathbf{U}$ are obtained for element e through:

$$\frac{\partial f_e^{(\xi)}}{\partial \bar{\xi}_e} = p_{f_\xi}\bar{\xi}_e^{p_{f_\xi}-1}f^{(1)} - p_{f_\xi}(1-\bar{\xi}_e)^{p_{f_\xi}-1}f^{(2)} \tag{C.13}$$

$$\frac{\partial f_e^{(\xi)}}{\partial \mathbf{U}} = \bar{\xi}_e^{p_{f_\xi}}\frac{\partial f^{(1)}}{\partial \mathbf{U}} + (1-\bar{\xi}_e)^{p_{f_\xi}}\frac{\partial f^{(2)}}{\partial \mathbf{U}} \tag{C.14}$$

$$\frac{\partial f^{(m)}}{\partial \mathbf{U}} = \left(\frac{\partial f^{(m)}}{\partial I_1^{(m)}}\frac{\partial I_1^{(m)}}{\partial \boldsymbol{\sigma}^{(m)}} + \frac{\partial f^{(m)}}{\partial J_2^{(m)}}\frac{\partial J_2^{(m)}}{\partial \boldsymbol{\sigma}^{(m)}} + \frac{\partial f^{(m)}}{\partial J_3^{(m)}}\frac{\partial J_3^{(m)}}{\partial \boldsymbol{\sigma}^{(m)}}\right)\cdot\frac{\partial \boldsymbol{\sigma}^{(m)}}{\partial \mathbf{U}} \quad m = 1, 2 \tag{C.15}$$

Here, $f^{(m)}$, $I_1^{(m)}$, $J_2^{(m)}$, and $J_3^{(m)}$ are obtained from the Cauchy stress $\boldsymbol{\sigma}^{(m)}$ corresponding to Material m ($m = 1, 2$) inside element e. For the detailed expressions of the gradients of single-material yield function with respect to the stress invariants and gradients of stress invariants with respect to Cauchy stress tensor, the readers are referred to [35]. The gradient of Cauchy stress tensor with respect to displacement vector is obtained as $\frac{\partial \boldsymbol{\sigma}^{(m)}}{\partial \mathbf{U}} = \mathbb{C}^{(m)}\mathbf{B}^{(m)}$, where $\mathbb{C}^{(m)}$ is the solid material constitutive matrix and $\mathbf{B}^{(m)}$ is the strain–displacement matrix of Material m ($m = 1, 2$).

Appendix D. Parameters for the augmented Lagrangian algorithm

The values of the AL parameters and convergence criteria for all numerical examples are listed in Table D.2. Lagrange multiplier estimators (λ_e) are updated after each AL step, and the penalty coefficient (μ) is updated when the average change in density design variable is below a prescribed tolerance.

Table D.2
AL parameters used in all the examples.

Parameter	Value
Initial Lagrange multiplier estimators, $\lambda_e^{(0)}$	0
Initial penalty coefficient, $\mu^{(0)}$	10
Maximum penalty coefficient, $\mu_{\max}$	10 000
Penalty update factor, α	1.05
Number of MMA iterations per AL step	5
Maximum number of AL steps	800 for 2D designs, and 160 for 3D designs
Convergence tolerance on density design variables	0.0015
Convergence tolerance on stress constraints	0.003

References

[1] J. Thomsen, Topology optimization of structures composed of one or two materials, Struct. Optim. 5 (1) (1992) 108–115, http://dx.doi.org/10.1007/BF01744703.

[2] O. Sigmund, S. Torquato, Design of materials with extreme thermal expansion using a three-phase topology optimization method, J. Mech. Phys. Solids 45 (6) (1997) 1037–1067, http://dx.doi.org/10.1016/S0022-5096(96)00114-7.

[3] J. Stegmann, E. Lund, Discrete material optimization of general composite shell structures, Internat. J. Numer. Methods Engrg. 62 (14) (2005) 2009–2027, http://dx.doi.org/10.1002/nme.1259.

[4] G.H. Yoon, Y.K. Park, Y.Y. Kim, Element stacking method for topology optimization with material-dependent boundary and loading conditions, J. Mech. Mater. Struct. 2 (2007) 883–895, http://dx.doi.org/10.2140/jomms.2007.2.883.

[5] L. Yin, G. Ananthasuresh, Topology optimization of compliant mechanisms with multiple materials using a peak function material interpolation scheme, Struct. Multidiscip. Optim. 23 (1) (2001) 49–62, http://dx.doi.org/10.1007/s00158-001-0165-z.

[6] T. Gao, W. Zhang, A mass constraint formulation for structural topology optimization with multiphase materials, Internat. J. Numer. Methods Engrg. 88 (8) (2011) 774–796, http://dx.doi.org/10.1002/nme.3197, arXiv:https://onlinelibrary.wiley.com/doi/pdf/10.1002/nme.3197. URL https://onlinelibrary.wiley.com/doi/abs/10.1002/nme.3197.

[7] M. Bruyneel, SFP—a new parameterization based on shape functions for optimal material selection: application to conventional composite plies, Struct. Multidiscip. Optim. 43 (1) (2011) 17–27, http://dx.doi.org/10.1007/s00158-010-0548-0.

[8] T. Gao, W. Zhang, P. Duysinx, A bi-value coding parameterization scheme for the discrete optimal orientation design of the composite laminate, Internat. J. Numer. Methods Engrg. 91 (1) (2012) 98–114, http://dx.doi.org/10.1002/nme.4270.

[9] W. Zuo, K. Saitou, Multi-material topology optimization using ordered SIMP interpolation, Struct. Multidiscip. Optim. 55 (2) (2017) 477–491, http://dx.doi.org/10.1007/s00158-016-1513-3.

[10] X.S. Zhang, G.H. Paulino, A.S. Ramos, Multi-material topology optimization with multiple volume constraints: a general approach applied to ground structures with material nonlinearity, Struct. Multidiscip. Optim. 57 (1) (2018) 161–182, http://dx.doi.org/10.1007/s00158-017-1768-3.

[11] Y. Zhou, T. Nomura, K. Saitou, Multi-component topology and material orientation design of composite structures (MTO-C), Comput. Methods Appl. Mech. Engrg. 342 (2018) 438–457, http://dx.doi.org/10.1016/j.cma.2018.07.039.

[12] X.S. Zhang, H. Chi, Efficient multi-material continuum topology optimization considering hyperelasticity: Achieving local feature control through regional constraints, Mech. Res. Commun. 105 (2020) 103494, http://dx.doi.org/10.1016/j.mechrescom.2020.103494, URL https://www.sciencedirect.com/science/article/pii/S0093641320300239.

[13] X.S. Zhang, H. Chi, G.H. Paulino, Adaptive multi-material topology optimization with hyperelastic materials under large deformations: A virtual element approach, Comput. Methods Appl. Mech. Engrg. 370 (2020) 112976, http://dx.doi.org/10.1016/j.cma.2020.112976.

[14] Z. Zhao, X.S. Zhang, Design of graded porous bone-like structures via a multi-material topology optimization approach, Struct. Multidiscip. Optim. 64 (2) (2021) 677–698, http://dx.doi.org/10.1007/s00158-021-02870-x.

[15] Z. Kang, L. Tong, Integrated optimization of material layout and control voltage for piezoelectric laminated plates, J. Intell. Mater. Syst. Struct. 19 (8) (2008) 889–904, http://dx.doi.org/10.1177/1045389X07084527, arXiv:https://doi.org/10.1177/1045389X07084527.

[16] Z. Luo, W. Gao, C. Song, Design of multi-phase piezoelectric actuators, J. Intell. Mater. Syst. Struct. 21 (18) (2010) 1851–1865, http://dx.doi.org/10.1177/1045389X10389345, arXiv:https://doi.org/10.1177/1045389X10389345.

[17] C. Zhuang, Z. Xiong, H. Ding, Topology optimization of multi-material for the heat conduction problem based on the level set method, Eng. Optim. 42 (9) (2010) 811–831, http://dx.doi.org/10.1080/03052150903443780.

[18] T. Gao, P. Xu, W. Zhang, Topology optimization of thermo-elastic structures with multiple materials under mass constraint, Comput. Struct. 173 (2016) 150–160, http://dx.doi.org/10.1016/j.compstruc.2016.06.002, URL https://www.sciencedirect.com/science/article/pii/S004579491630431X.
[19] H. Ghasemi, H.S. Park, T. Rabczuk, A multi-material level set-based topology optimization of flexoelectric composites, Comput. Methods Appl. Mech. Engrg. 332 (2018) 47–62, http://dx.doi.org/10.1016/j.cma.2017.12.005, URL https://www.sciencedirect.com/science/article/pii/S0045782517307569.
[20] A. Takezawa, M. Kobashi, Design methodology for porous composites with tunable thermal expansion produced by multi-material topology optimization and additive manufacturing, Composites B 131 (2017) 21–29, http://dx.doi.org/10.1016/j.compositesb.2017.07.054.
[21] G. Zhang, K. Khandelwal, Computational design of finite strain auxetic metamaterials via topology optimization and nonlinear homogenization, Comput. Methods Appl. Mech. Engrg. 356 (2019) 490–527, http://dx.doi.org/10.1016/j.cma.2019.07.027.
[22] W. Li, F. Wang, O. Sigmund, X.S. Zhang, Design of composite structures with programmable elastic responses under finite deformations, J. Mech. Phys. Solids 151 (2021) 104356, http://dx.doi.org/10.1016/j.jmps.2021.104356, URL https://www.sciencedirect.com/science/article/pii/S0022509621000533.
[23] S.H. Jeong, D.-H. Choi, G.H. Yoon, Separable stress interpolation scheme for stress-based topology optimization with multiple homogeneous materials, Finite Elem. Anal. Des. 82 (2014) 16–31, http://dx.doi.org/10.1016/j.finel.2013.12.003, URL https://www.sciencedirect.com/science/article/pii/S0168874X13002138.
[24] S. Xu, J. Liu, B. Zou, Q. Li, Y. Ma, Stress constrained multi-material topology optimization with the ordered SIMP method, Comput. Methods Appl. Mech. Engrg. 373 (2021) 113453, http://dx.doi.org/10.1016/j.cma.2020.113453, URL https://www.sciencedirect.com/science/article/pii/S0045782520306381.
[25] X. Guo, W. Zhang, W. Zhong, Stress-related topology optimization of continuum structures involving multi-phase materials, Comput. Methods Appl. Mech. Engrg. 268 (2014) 632–655, http://dx.doi.org/10.1016/j.cma.2013.10.003, URL https://www.sciencedirect.com/science/article/pii/S0045782513002557.
[26] S. Chu, L. Gao, M. Xiao, Z. Luo, H. Li, Stress-based multi-material topology optimization of compliant mechanisms, Internat. J. Numer. Methods Engrg. 113 (7) (2018) 1021–1044, http://dx.doi.org/10.1002/nme.5697, arXiv:https://onlinelibrary.wiley.com/doi/pdf/10.1002/nme.5697. URL https://onlinelibrary.wiley.com/doi/abs/10.1002/nme.5697.
[27] M.P. Bendsøe, O. Sigmund, Material interpolation schemes in topology optimization, Arch. Appl. Mech. 69 (9) (1999) 635–654, http://dx.doi.org/10.1007/s004190050248.
[28] O. Sigmund, Design of multiphysics actuators using topology optimization – part II: Two-material structures, Comput. Methods Appl. Mech. Engrg. 190 (49) (2001) 6605–6627, http://dx.doi.org/10.1016/S0045-7825(01)00252-3.
[29] T.E. Bruns, D.A. Tortorelli, Topology optimization of non-linear elastic structures and compliant mechanisms, Comput. Methods Appl. Mech. Engrg. 190 (26) (2001) 3443–3459, http://dx.doi.org/10.1016/S0045-7825(00)00278-4.
[30] B. Bourdin, Filters in topology optimization, Internat. J. Numer. Methods Engrg. 50 (9) (2001) 2143–2158, http://dx.doi.org/10.1002/nme.116.
[31] O. Sigmund, Morphology-based black and white filters for topology optimization, Struct. Multidiscip. Optim. 33 (4) (2007) 401–424, http://dx.doi.org/10.1007/s00158-006-0087-x.
[32] F. Wang, B.S. Lazarov, O. Sigmund, On projection methods, convergence and robust formulations in topology optimization, Struct. Multidiscip. Optim. 43 (6) (2011) 767–784, http://dx.doi.org/10.1007/s00158-010-0602-y.
[33] M. Zhou, G. Rozvany, The COC algorithm, part II: Topological, geometrical and generalized shape optimization, Comput. Methods Appl. Mech. Engrg. 89 (1–3) (1991) 309–336.
[34] M.P. Bendsøe, O. Sigmund, Topology Optimization: Theory, Methods and Applications, Springer, Berlin, Heidelberg, 2003, http://dx.doi.org/10.1007/978-3-662-05086-6.
[35] O. Giraldo-Londoño, G.H. Paulino, A unified approach for topology optimization with local stress constraints considering various failure criteria: von mises, drucker–prager, tresca, mohr–Coulomb, bresler– pister and willam–warnke, Proc. R. Soc. A (2020) http://dx.doi.org/10.1098/rspa.2019.0861, 4762019086120190861.
[36] R.v. Mises, Mechanik der festen Körper im plastisch- deformablen zustand, Nachr. Ges. Wiss. Gött. Math. Phys. Klasse 4 (1913) 582–592, URL http://eudml.org/doc/58894.
[37] D.C. Drucker, W. Prager, Soil mechanics and plastic analysis or limit design, Quart. Appl. Math. 10 (1952) 157–165, http://dx.doi.org/10.1090/qam/48291.
[38] M.A. Eddings, M.A. Johnson, B.K. Gale, Determining the optimal PDMS–PDMS bonding technique for microfluidic devices, J. Micromech. Microeng. 18 (6) (2008) 067001, http://dx.doi.org/10.1088/0960-1317/18/6/067001.
[39] W. Li, F. Wang, O. Sigmund, X.S. Zhang, Digital synthesis of free-form multimaterial structures for realization of arbitrary programmed mechanical responses, Proc. Natl. Acad. Sci. 119 (10) (2022) e2120563119, http://dx.doi.org/10.1073/pnas.2120563119, URL https://www.pnas.org/doi/abs/10.1073/pnas.2120563119.
[40] P. Duysinx, O. Sigmund, New developments in handling stress constraints in optimal material distribution, in: 7th AIAA/USAF/NASA/ISSMO Symposium on Multidisciplinary Analysis and Optimization, American Institute of Aeronautics and Astronautics, 1998, http://dx.doi.org/10.2514/6.1998-4906, 0.
[41] O. Giraldo-Londoño, G.H. Paulino, PolyStress: a matlab implementation for local stress-constrained topology optimization using the augmented Lagrangian method, Struct. Multidiscip. Optim. 63 (4) (2021) 2065–2097, http://dx.doi.org/10.1007/s00158-020-02760-8.
[42] D.P. Bertsekas, Nonlinear Programming, Athena Scientific, Belmont, MA, 1999.
[43] J. Nocedal, S. Wright, Numerical Optimization, Springer, New York, NY, 2006, http://dx.doi.org/10.1007/978-0-387-40065-5.
[44] J. Pereira, E. Fancello, C. Barcellos, Topology optimization of continuum structures with material failure constraints, Struct. Multidiscip. Optim. 26 (1–2) (2004) 50–66.
[45] E.A. Fancello, Topology optimization for minimum mass design considering local failure constraints and contact boundary conditions, Struct. Multidiscip. Optim. 32 (3) (2006) 229–240, http://dx.doi.org/10.1007/s00158-006-0019-9.
[46] H. Emmendoerfer, E.A. Fancello, A level set approach for topology optimization with local stress constraints, Internat. J. Numer. Methods Engrg. 99 (2) (2014) 129–156.
[47] H. Emmendoerfer, E.A. Fancello, Topology optimization with local stress constraint based on level set evolution via reaction–diffusion, Comput. Methods Appl. Mech. Engrg. 305 (2016) 62–88.
[48] H. Emmendoerfer, E.C.N. Silva, E.A. Fancello, Stress-constrained level set topology optimization for design-dependent pressure load problems, Comput. Methods Appl. Mech. Engrg. 344 (2019) 569–601, http://dx.doi.org/10.1016/j.cma.2018.10.004, URL https://www.sciencedirect.com/science/article/pii/S0045782518305000.
[49] G.A. da Silva, A.T. Beck, E.L. Cardoso, Topology optimization of continuum structures with stress constraints and uncertainties in loading, Internat. J. Numer. Methods Engrg. 113 (1) (2018) 153–178, http://dx.doi.org/10.1002/nme.5607, arXiv:https://onlinelibrary.wiley.com/doi/pdf/10.1002/nme.5607. URL https://onlinelibrary.wiley.com/doi/abs/10.1002/nme.5607.
[50] G.A. da Silva, A.T. Beck, O. Sigmund, Stress-constrained topology optimization considering uniform manufacturing uncertainties, Comput. Methods Appl. Mech. Engrg. 344 (2019) 512–537, http://dx.doi.org/10.1016/j.cma.2018.10.020, URL https://www.sciencedirect.com/science/article/pii/S0045782518305231.
[51] G.A. da Silva, A.T. Beck, O. Sigmund, Topology optimization of compliant mechanisms considering stress constraints, manufacturing uncertainty and geometric nonlinearity, Comput. Methods Appl. Mech. Engrg. 365 (2020) 112972, http://dx.doi.org/10.1016/j.cma.2020.112972, URL https://www.sciencedirect.com/science/article/pii/S0045782520301559.
[52] F.V. Senhora, O. Giraldo-Londoño, I.F.M. Menezes, G.H. Paulino, Topology optimization with local stress constraints: a stress aggregation-free approach, Struct. Multidiscip. Optim. 62 (4) (2020) 1639–1668, http://dx.doi.org/10.1007/s00158-020-02573-9.
[53] G.A. da Silva, N. Aage, A.T. Beck, O. Sigmund, Three-dimensional manufacturing tolerant topology optimization with hundreds of millions of local stress constraints, Internat. J. Numer. Methods Engrg. 122 (2) (2021) 548–578, http://dx.doi.org/10.1002/nme.6548, arXiv:https://onlinelibrary.wiley.com/doi/pdf/10.1002/nme.6548. URL https://onlinelibrary.wiley.com/doi/abs/10.1002/nme.6548.
[54] K. Svanberg, The method of moving asymptotes—a new method for structural optimization, Internat. J. Numer. Methods Engrg. 24 (2) (1987) 359–373, http://dx.doi.org/10.1002/nme.1620240207.
[55] H. Tresca, Me Moires sur l'e Coulement des Corps Solides, Imprimerie impe riale, Paris, France, 1869.
[56] C. Coulomb, Essai sur une application des regles de maximis et minimis quelques problemes de statique, relatits a l'architecture, Mem. Math. l'Acad. R. Sci. 7 (1776).